Hydromechanical coupling in response to earthquakes: on the possible consequences for aftershocks

Pierre Gavrilenko

Geophys. J. Int. (2005) **161,** 113–129 doi: 10.1111/j.1365-246X.2005.02538.x

Hydromechanical coupling in response to earthquakes: on the possible consequences for aftershocks

Pierre Gavrilenko

Geosciences Rennes, UPR 4661, *CNRS, Rennes, France. E-mail: Pierre.Gavrilenko@univ-rennes1.fr*

Accepted 2004 November 1. Received 2004 October 22; in original form 2003 September 3

SUMMARY

Numerous observations indicate that fluids circulate in the crust after an earthquake, with time constants comparable to those of the aftershocks. This paper provides new viewpoints concerning the relationship between the fluid flow and aftershocks. The fault on which the main quake occurs is modelled using a rectangular dislocation surface that is embedded in a 3-D poroelastic half-space. The main event is modelled by prescribing a given amount of displacement over the dislocation surface which results in deformation throughout the surrounding crust. The fluid redistribution that then ensues is modelled using the equations of poroelasticity. We show that this process can lead to time-dependent weakening effects. The results are analysed in terms of how changes in a Coulomb failure function (ΔCFF) evolve through time. The spatial and temporal distributions of aftershocks triggered by ΔCFF are modelled on a statistical basis. We test our model in various situations. The spatial distribution of aftershocks is depicted in various tectonic environments and we show that the fluid flow seemingly provides a convincing mechanism for the triggering of aftershocks. Both off-fault aftershocks and aftershocks close to the surface rupture have been modelled. We have also investigated the condition under which the Omori decay law (and its associated time exponent p) is expected and we show that the permeability should vary within a window of less than two orders of magnitude in order to match the observed value of $p \approx 1$. With seismic data from the Northridge event (1994), we show that a crustal permeability of 7.5×10^{-15} m^2 allows us to describe quite well the time dependence of the aftershock. However, the permeability should vary proportionally to L^2, where L is the scale length over which the fluid-pressure equilibration occurs that is dependent on the size of the main event, in order to obtain a similar decay law ($p \approx 1$) at every scale (main-event magnitude). Finally, the link with the post-seismic hydrological observations is established and we show that the fluid flow predicted in the model of the Northridge event is consistent within an order of magnitude with field observations reported by Muir-Wood & King.

Key words: aftershocks, fluid flow, hydrological anomalies, poroelastic coupling, stress transfer.

1 INTRODUCTION

Many physical measurements are made during a series of seismic events in order to monitor physical anomalies due to precursory and/or post-seismic effects. Detection of precursory effects is one of these measurements that remains elusive. However, numerous post-seismic effects have been observed. By studying the post-seismic response of the crust, one hopes to gain a better understanding of the physical processes responsible for seismicity in general and aftershocks in particular. Concerning the effects of the fluids, the conditions under which the fluids circulate in the fault zone remain poorly known as does the exact role that the fluids may play both before and after the main event. Although fluids may be involved in many physical and chemical processes, we will focus here on the mechanical and hydrological consequences of fluid-pressure equilibration following a main event.

1.1 Fluid flow and mechanical processes following earthquakes

Fluid-assisted mechanical processes have been studied for a long time. In the 1970s, dilatancy as a possible precursor process gained much attention (Nur 1972; Scholz *et al.* 1973). However, despite a few notable successes (e.g. Aggarwal *et al.* 1973), observations in the field have not confirmed the predictions. The post-seismic response of principal interest is the spatial and temporal

distribution of aftershocks. Aftershock sequences have been recorded for many years. Even though a high level of confidence can now be attached to the precision of the data, the physical mechanisms governing aftershocks remain uncertain. Models have generally been unsuccessful in explaining the entire range of spatial and temporal features exhibited by aftershocks.

Usually, the rate of aftershock occurrence after an earthquake is well described using the Omori law Utsu *et al.* (1995):

$$n(t) = K_0 \big/ [c + (t - t_0)]^p \tag{1}$$

where $n(t)$ represents the number of aftershocks per unit time interval at time t, K_0 and c are two constants, t_0 is the time of the main event and p is the Omori exponent which is usually found to be around 1. Let us note that the unit time interval for calculating the rate of aftershock occurrence is usually 1 day. However, it may be lowered to a few hours depending on the quality of the aftershock catalogue.

In some cases the actual sequence of aftershocks deviates from the Omori law. The so-called epidemic-type aftershock sequence (ETAS) is a noticeable example of this deviation (Ogata 1988). In this case, at least some aftershocks yield new sequences of aftershocks and the deviation from the Omori law can be directly related to the occurrence of some large aftershocks. However Correig *et al.* (1997) reported observations of aftershock sequences not correlating with any particular large event. Moreno *et al.* (2001) showed that the pattern of aftershocks can fall into two categories: (1) some leading events which match the Omori law with the exponent $p = 0.94$ and (2) a cascade of events which follow the leading events and exhibits $p \approx 0.7$. The main point is that the so-called 'leading' events do not display any remarkable features. As suggested by Moreno *et al.* (2001), the Omori law appears to be a type of first approximation to the decay of aftershock activity.

Various models have been proposed to explain the appearance of aftershocks. The first class of model involves a physical process including a time-dependent behaviour which matches the Omori law. Dieterich (1994) analysed the aftershock process by considering time-dependent nucleation models. Starting from the constitutive equations of time-dependent friction, he showed that the stress changes associated with a major event induce a series of earthquakes that follow the Omori law with $p = 1$. However, deviations from this behaviour are expected, since Dieterich (1994) considered a uniform spatial stress change. Assuming a more complex (non-uniform) stress change, p reduces to 0.8. More complex behaviour associated with, for example, creep effects and history-dependent stress changes could lead to various Omori exponents different from 1. As noticed by Dieterich (1994), time-dependent nucleation processes may not be required to explain the temporal decay of aftershocks if other effects such as viscoelastic or poroelastic processes are taken into account.

The spring-block models, initially developed by Burridge & Knopoff (1967) to describe the Gutenberg–Richter power-law distribution, have received a great deal of interest as a means of reproducing the complexity of seismological observations. Within this framework, many researchers have attempted to derive aftershock sequences from spring-block models. Dieterich (1972) concluded that it was possible to generate aftershock sequences by considering a viscoelastic rheology within the fault zone, as well as time-dependent friction. These aftershocks were found to follow the Omori law. Nakanishi (1992) came to a similar conclusion by considering a viscoelastic relaxation under the fault. Hainzl *et al.* (1999) have further investigated the viscoelastic coupling between the sliding blocks and blocks situated in the immediate neighbourhood. They found that such spring-block models allow a simulation of both foreshock and aftershock sequences with the appropriate power-law distributions. In addition, they found that the Omori exponent should depend on the relaxation time constant of the viscoelastic process. Moreover, the distribution of magnitude of the aftershocks matches the Gutenberg–Richter law well. However, the aftershocks in these models of spring blocks are located on or near the fault plane. An alternative to the models of viscoelastic relaxation/time-dependent friction has been proposed by Scholz (1968) with an extrapolation of the laboratory results to the crustal scale. Taking the static fatigue resulting from the stress corrosion into account, Scholz showed that the Omori law can be derived using simple assumptions. However, the question is to find how these mechanisms may be extrapolated to the field scale.

Nur & Booker (1971) have suggested another weakening mechanism. The weakening effect is assumed to result from the redistribution of fluid associated with the strain field which takes place when the fault slides. The fluid diffuses from compressed regions to dilated ones with a time constant depending on the fluid-pressure diffusivity of the porous medium. Assuming that slip is controlled by a Coulomb criterion, Nur & Booker (1971) express the change in fault strength S as:

$$\Delta S = -\mu(\Delta\sigma_{kk}/3 + \Delta P) \tag{2}$$

where $\sigma_{kk}/3$ is the mean normal stress, P is the pore pressure and μ is the friction coefficient of faults (note that throughout this paper we define compressive stress as being negative). According to eq. (2), we find the well-known result that an increase in the compressive stress ($\Delta\sigma_{kk}/3 < 0$) leads to consolidation ($\Delta S > 0$) whereas an increase in fluid pressure ($\Delta P > 0$) weakens the fault ($\Delta S < 0$).

In order to clarify the underlying physics, it is worth decomposing ΔP into two terms:

$$\Delta P = \Delta P_{\mathrm{u}} + \delta P(t). \tag{3}$$

The first term ΔP_u corresponds to the pressure change in the undrained fluid as a result of the change in $\sigma_{kk}/3$ at the time of occurrence of the earthquake $t = t_0$. By definition, this term does not change with time. This term can be easily calculated using the following relation: $\Delta P_{\mathrm{u}} = -B\ \Delta\sigma_{kk}/3$, where B is called the Skempton coefficient. The second term $\delta P(t)$ is time dependent and is related to the diffusion process. At $t = t_0$,$\delta P(t) = 0$.

Assuming for simplicity a Skempton coefficient $B = 1$ (i.e. $\Delta P_{\mathrm{u}} = -\Delta\sigma_{kk}/3$), the mechanical resistance is $\Delta S = 0$ everywhere just after the event. Then fluid pressure relaxes through the diffusion process and the mechanical resistance is given by $\Delta S = -\mu\delta P(t)$. In a compressed region, $\delta P(t)$ decreases with time from 0 to $-\Delta P_{\mathrm{u}} (< 0)$. As a consequence ΔS increases in the compressed region which leads to consolidation. In the dilated area, $\delta P(t)$ increases from 0 to $-\Delta P_{\mathrm{u}} (> 0$, since $\Delta P_{\mathrm{u}} < 0$ in the dilated area) and thus ΔS decreases with time indicating that the medium weakens.

Nur & Booker (1971) considered the stress field resulting from an edge dislocation. Assuming that the number of aftershocks between t and $t + dt$ is proportional to the increment of the fluid pressure $\delta P(t+dt) - \delta P(t)$, they found an Omori type law with an exponent $p = 0.5$. Although those authors recognized that the model predicts a cluster of aftershocks near the end of the fault, they pointed out that a volumetric change around the fault plane can generate aftershocks along that fault. Even though the physical mechanism responsible for the aftershocks is clearly explained, the effect of shear stress is not accounted for. This model provides information on how the Mohr circle moves with regard to the failure envelope, but puts aside the possible consolidation of the medium in response to the drop in the shear stress.

The influence of the static stress field on the spatial distribution of aftershocks has been thoroughly investigated by Stein & Lisowski (1983). A relevant concept for the study of the relationship between the static stress change and the failure is the concept of the change in the Coulomb failure function (denoted ΔCFF). Various authors attempted to map the change in Coulomb failure function associated with earthquakes which is defined as $\Delta\mathrm{CFF} = \Delta\tau + \mu'\Delta\sigma_n$ where τ and σ_n are, respectively, the shear and the normal stress acting on the fault and $\mu' = \mu(1 - B)$ is an apparent friction coefficient accounting for the presence of fluid through the Skempton coefficient B. When $\Delta\mathrm{CFF} > 0$, a fault is brought closer to failure, while when $\Delta\mathrm{CFF} < 0$ the fault is stabilized. Stein & Lisowski (1983) found that aftershocks occur preferentially where the Coulomb stresses increase and correlate well in places when the increase is more than 0.3 MPa. Further, a Coulomb stress drop of a few tenths of a megapascal generally prevents the occurrence of aftershocks. According to the same authors, the aftershocks occur at such a distance that the increase in Coulomb stress is in the range 0.05–0.1 MPa. Another important feature is that the Coulomb stress increases most in dilated regions; this is confirmed by the observation of aftershock distribution. King *et al.* (1994) have developed similar ideas and found the same type of correlation between increase in Coulomb stress and aftershocks. This has led various authors to superimpose the spatial distribution of aftershocks on the zones where the Coulomb stresses increase. Wang & Chen (2001) found that the coincidence between both spatial distribution is about 67 per cent for the Chi-Chi earthquake (which occurred in Taiwan in 1999). Although they conclude that such a percentage may not be random, we may wonder why aftershocks also occurred in zones where the Coulomb stresses decreased. Finally, the following is a questionable aspect of this approach: taking the Skempton coefficient into account means that the authors have considered a change in pressure of undrained fluid which results from the static stress variation. Thus, they have not taken fluid flow into account. Thus, everything happens as if the time constant for fluid flow was much larger than the time constant for the relaxation of aftershocks; i.e. as if diffusivity was low enough to preclude the fluid flow at these time constants. Moreover, the authors who deal with static stress change do not provide any time-dependent mechanism to allow for a delayed rupture.

Li *et al.* (1987) deal with the problem of aftershocks within the same framework as Nur & Booker (1971) by considering the fluid flow effect and the associated spatial and time variation of the Coulomb stress. Although it is not necessarily conclusive, the paper by Li *et al.* (1987) provides some keys to a better understanding of the mechanics of aftershocks in relation to the redistribution of stresses. They make a strike-slip model by considering a sudden introduction of a distribution of edge dislocations embedded into a 2-D medium. Then, they consider the result of variation of Coulomb stress with time. The fact that the aftershock zone is likely to extend as the fluid flows from the compressed area into the dilated one is an improved result. The questionable point concerns a possible correlation between the distance where aftershocks occur and the variation in Coulomb stress with time. Li *et al.* (1987) obtained seismic data on various time windows indicating that the number of aftershocks away from the main shock seems to increase with time. Although this trend must be taken cautiously due to the inaccuracy in aftershock determination, at least it is consistent with the fluid flow model.

The poroelastic analysis has been proposed again recently by Bosl & Nur (2002) in the case of the 1992 Landers earthquake. It provides convincing evidence that accounting for the poroelastic response of the porous medium may significantly improve the relationship between the positive Coulomb stress and the occurrence of aftershocks. Bosl & Nur (2002) found that 87 per cent of the aftershock events correspond to a positive Coulomb stress at the time of the event. The average Coulomb stress was 0.155 MPa and the permeability of the crust was set to $k = 1$ mD $= 10^{-15}$ m^2.

1.2 Hydrological change following earthquakes

Changes in water level have been recognized for a long time as anomalies reflecting stress variations in the crust. As far as co-seismic changes are concerned, there are many occasions where the changes in water level in wells are consistent with the tectonic deformation. Grecksch *et al.* (1999) showed a good example where the sign in the co-seismic change in water level matches quite well the pattern of crustal deformation. However, there are many cases where the amplitude of observed water level changes is strongly different from what is expected from the strain sensitivity of the water level in wells. For instance, Galloway *et al.* (1994) found a discrepancy of about two orders of magnitude between the observed response in a well situated at a distance of 400 km and the expected one. This discrepancy has not yet received a good explanation but it clearly questions the capacity for change in water level to reflect tectonic processes. Kuempel (1992) raises a similar question about the precursor effect. Indeed it appears in most cases that precursory changes in water level cannot be attributed to fluid flow from the focal area. A major challenge is to properly allow for the heterogeneity of the crustal response. Thus, according to Kuempel (1992), the changes in water level induced by fluid mobilization following an earthquake should be observed only in the focal area.

Considering post-seismic fluid flow, Muir-Wood & King (1987) reported a number of observations of anomalous fluid regimes in the rivers and springs in the focal area. According to their observations, the anomalies correlated well with the deformation patterns associated with the earthquakes. Moreover the time constant of these anomalies was around 6 to 12 months, involving fluid volumes as large as 0.5 km^3. A crude model was used by Muir-Wood & King (1987) to interpret these observations. They found that the fluids down to at least the first 5 km depth should be mobilized to explain the large volumes of expelled fluid. In an interesting study, Rojstaczer *et al.* (1995) focused on a particular well in the same area to give quite a different explanation for the observed anomalies and to favour to a local permeability increase. We shall notice that local modification of the fluid flow paths has often been used to explain the anomalous behaviour of water levels (e.g. Leonardi *et al.* 1997; Roeloffs 1998; Gavrilenko *et al.* 2000). Even though the correlation between the fluid flow anomalies and the deformation is not perfect, it nonetheless provides a strong argument in favour of a tectonically driven fluid flow in the focal area. The compilation of Muir-Wood & King (1987) offers much more direct evidence of this process.

A more recent analysis of synthetic aperture radar (SAR) data by Peltzer *et al.* (1998) provides complementary evidence, even though indirect, of this phenomenon. Using SAR measurements over a period of 4 yr, they showed that post-seismic slip cannot account for the vertical displacement evidenced by SAR. They analysed the deformation field by considering a poroelastic rebound, in which the Poisson coefficient varies from the undrained value $\nu_u = 0.35$ down to the drained one $\nu = 0.27$ with a time constant equal to 0.75 yr. According to the paper by Peltzer *et al.* (1998), this time constant is consistent with the mechanical changes that are associated with the occurrence of aftershocks, as well as the hydrological observations of Muir-Wood & King (1987).

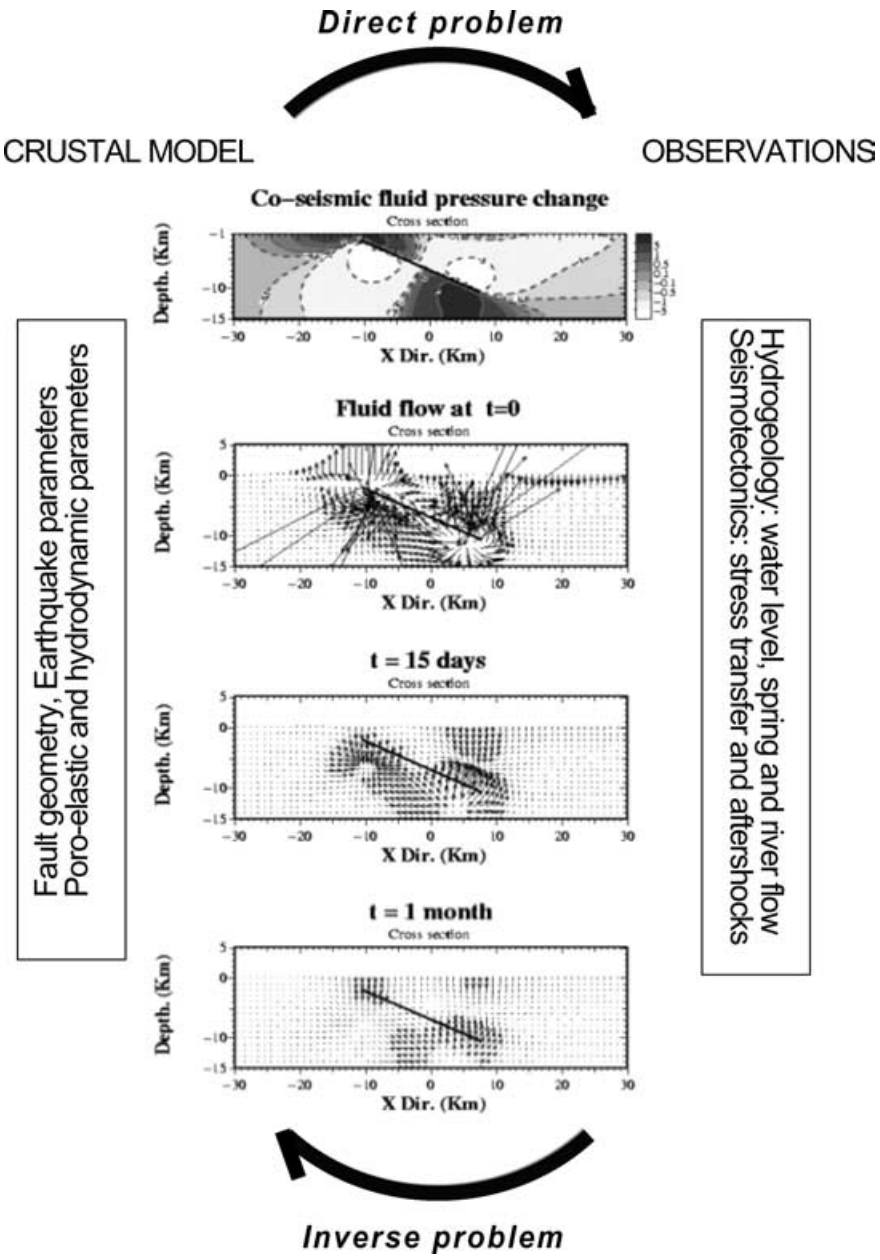

Figure 1. Summary of the problem. Sketch diagram showing the physical processes at three time steps. The model parameters are indicated on the left-hand side and the observable variables on the right-hand side. The arrows indicate both the direct and the inverse problem to be solved.

1.3 Position of the problem

The aim of this paper is to provide a new viewpoint on the relationship between fluid flow and the hydromechanical observations following earthquakes. We will examine in more detail the possible effect of fluid flow. Considering the time constants which are derived by Muir-Wood & King (1987) and by Peltzer *et al.* (1998) fluid flow is expected to generate significant post-seismic hydromechanical changes. We investigate how fluid flow may account for the spatial and temporal distribution of the aftershocks and determine what the crustal hydrodynamic requirements are. The approach is mainly numerical and is summarized in Fig. 1. Details of the modelling are provided in the next section.

We consider a fault which slides at a given time t_0. As a consequence of the seismic event, the fluid will flow from compressed regions to dilated ones, as shown in Fig. 1, for three values of time. The direct problem consists of choosing the fault parameters and the hydrodynamic properties and then studying the possible effect of the resulting fluid flow in terms of both the hydrological changes and the mechanical changes. The hydrological changes mainly deal with the variation of the water level in wells as well as the variations in river discharges. The mechanical changes are due to stress transfer and the possible triggering of the aftershocks. Results of the modelling may be then compared with field observations. In this paper we will present mainly the direct problem. We will investigate the hydrological conditions under which aftershocks may be expected to occur, and what we can predict about their spatial and temporal distribution.

The inverse problem is to start with the observations of hydrological and mechanical changes and extract the pertinent

hydrodynamic parameters for the fault area. First, we are going to present a very crude approach based on the seismological data of the 1994 Northridge earthquake. The hydrological consequences using the extracted hydrodynamic parameters are then drawn in order to fix the order of magnitude for the expected effects.

2 BASIC MODEL

We present here a model to describe fluid flow as a response to a seismic event. We assume a crust composed of a permeable top layer saturated with fluids and behaving like a poroelastic medium. It lies over a lower crustal layer which is considered as an elastic impermeable medium. The fact that the lower layer is impermeable is rather intuitive, since the paths for fluid flow are progressively destroyed by the combined effects of pressure and temperature. However, the depth of the interface between the upper permeable layer and the lower impermeable layer is unknown.

In the following, we will consider that fluids are free to circulate down to 15 km. The lower elastic crust in this model is probably oversimplified and does not take into account the possible recovery of stress by viscoelastic relaxation. However, the role of viscoelastic relaxation is not the focus of the present study. Assuming that a seismic event occurs at a given time t_0, how do we account for this event as far as fluid flow is concerned? First, we are going to present the equations governing the fluid flow associated with the seismic disturbance. Then we are going to display the fault model used to describe the seismic event and the crustal parameters. This basic model is supplemented later by a description of the mechanical strength of the medium. Once all the parameters of the model are introduced, the later evolution of the model, and in particular the possible triggering of aftershocks by fluid flow, can be studied.

2.1 Governing equations, boundary conditions and numerical aspects

2.1.1 Poroelastic equations

We use here the formalism and notations of Rice & Cleary (1976) which are generally valid for coupled mechanical processes in fluid-saturated porous media. Since stress and fluid flow are fully coupled, we need to describe both the fluid pressure and the variation of stress with time. This is done by using the coupled poroelastic equations which govern the behaviour of the medium as expressed by Rice & Cleary (1976). The constitutive equations are:

$$2G\epsilon_{ij} = \sigma_{i,j} - \frac{\nu}{1+\nu}\sigma_{kk}\delta_{ij} + \frac{3(\nu_u - \nu)}{B(1+\nu)(1+\nu_u)}p\delta_{ij} \tag{4}$$

and

$$m - m_0 = 3\frac{\rho_0(\nu_u - \nu)}{2GB(1+\nu)(1+\nu_u)}(\sigma_{kk} + 3P/B) \tag{5}$$

where ϵ_{ij} and σ_{ij} are respectively the strain and the stress tensor, P is the pore pressure, m is the fluid mass content per unit volume of porous material, m_0 refers to a reference state, G is the (fluid-independent) shear modulus, ν and ν_u are respectively the Poisson's coefficient of the drained and undrained rock and B is the Skempton coefficient (fluid pressure divided by confining pressure under undrained conditions).

Using the compatibility equations of elasticity, along with the conservation of fluid mass:

$$\partial q_i/\partial x_i + \partial m/\partial t = 0, \tag{6}$$

and Darcy's law:

$$q_i = -\rho_0(k/\eta)\partial p/\partial x_i \tag{7}$$

where q_i is the fluid mass flow rate, k is the permeability and η is the fluid viscosity, Rice & Cleary (1976) derive the equation for the diffusion of fluid mass:

$$c_m\nabla^2 m = \partial m/\partial t. \tag{8}$$

The diffusivity c_m is given by:

$$c_m = \frac{k}{\eta}\frac{2GB^2}{9}\frac{(1+\nu_u)^2(1-\nu)}{(1-\nu_u)(\nu_u - \nu)}. \tag{9}$$

At this stage we deviate slightly from the approach of Rice & Cleary (1976) and note that our analysis is occurring, effectively, in a uniform poroelastic half-space. In this case of a uniform material having an infinite lateral extent, Pride *et al.* (2004) have shown that an exact result exists between the fluid-pressure induced changes in the confining pressure $\delta\sigma_{kk}/3$ and the diffusive contribution of fluid pressure change ΔP (see eq. 3); namely, $\delta\sigma_{kk}/(3\times\delta P) = 2(\nu_u - \nu)/[B(1+\nu_u)(1-\nu)]$. Thus, the diffusion equation for the fluid mass can be written as a diffusion equation for the fluid pressure:

$$c_m\nabla^2 P = \partial P/\partial t. \tag{10}$$

The initial data and boundary conditions required for determining P are discussed in the next subsection.

Given a solution for P (and therefore $\delta\sigma_{kk}$), Pride *et al.* (2004) have shown how to determine the remaining deviatoric response of the material as the solution of a Poisson equation for the material displacements. However, the changes in the deviatoric stress tensor caused by the fluid-pressure diffusion are quite small, and in a first analysis we elect to neglect the variation in time of the deviatoric stress.

2.1.2 Boundary and initial conditions

At $t = t_0$, the changes in fluid pressure ΔP and in mean normal stress $\Delta\sigma_{kk}$ are related through the Skempton coefficient using the relation:

$$\Delta P_{(t=t_0)} = -B\Delta\sigma_{kk}/3. \tag{11}$$

The mean normal stress change is calculated using the stress field derived from a dislocation model as we will see in the next section. The spatial conditions at the boundaries of the discretized volume are as follows:

(i) Impermeable conditions are imposed at the basement of the upper fluid connected layer and thus we have

$$\partial P/\partial z = 0. \tag{12}$$

(ii) The free surface boundary at $z = 0$ imposes the condition

$$P_{(z=0)} = 0. \tag{13}$$

(iii) Finally the vertical boundaries are chosen far enough away to be undisturbed when the earthquake occurs, so that

$$\Delta P \approx 0. \tag{14}$$

2.1.3 Numerical procedure

The crust is discretized using a 3-D rectangular mesh. The mesh size is usually chosen to be around 1 km which is thought to be a good

Table 1. Table of the poroelastic and hydrodynamic parameters used in numerical models.

	Model parameters	Numerical value
Input	ν_u	0.25
	G	3.0×10^{10} Pa
	K	5.0×10^{10} Pa
	K_f	3.33×10^{9} Pa
	Φ	0.01
	$(1/\Phi)\,(d\Phi/dP)$	1.9×10^{-9} Pa^{-1}
	k	5.0×10^{-15} m^2
Calculated	B	0.85
	ν_u	0.34
	K_u	8.4×10^{10} Pa
	c_m	2 m^2 s^{-1}

compromise between the need to catch the variations in fluid pressure and the requirement to deal with tractable numerical problems. Eq. (10) is solved using a finite-difference scheme and applying the boundary conditions (11), (12), (13) and (14). We used here the alternating direction implicit algorithm of Douglas & Rachford (1956) which is unconditionally stable.

2.2 Physical modelling

2.2.1 Crustal model

In the simulations displayed in the next section, in order to simplify, we further neglect the pressure dependence of permeability. The permeability k is considered as uniform throughout the upper crustal layer. Nevertheless, we need to consider a pressure dependence of porosity in order to calculate the undrained Poisson coefficient ν_u, the Skempton coefficient B and finally the diffusion coefficient c_m. Using the pore compressibility $(1/\Phi)\,(d\Phi/dP)$ and the elastic coefficients we were able to calculate the poroelastic coefficients starting from the relations given by Rice & Cleary (1976):

$$B = \frac{1/K - 1/K_s}{1/K - 1/K_s + \Phi(1/K_f - 1/K_s)} \tag{15}$$

and

$$\nu_u = \frac{3\nu_u + B(1-2\nu_u)(1-K/K_s)}{3 - B(1-2\nu_u)(1-K/K_s)} \tag{16}$$

where K is the drained bulk modulus, K_s is the bulk modulus of the solid phase and K_f is the bulk modulus of the fluid. An example of the poroelastic parameters that we will use in our simulations is given in Table 1.

With regard to the geometrical fault characteristics and the tectonic setting we will explore simple but contrasting situations. Many parameters influencing the aftershock pattern could (and should) be considered. One of the main goals of our paper is not to investigate complex situations close to geological reality but to make some preliminary remarks on the influence of various parameters of the model. We will mainly consider focal mechanisms (pure strike-slip and reverse faults), the orientation of faults and the distribution of slip along the faults.

2.2.2 Fault model and tectonic setting

The basic fault model considers a rectangular dislocation buried in a 3-D half-space. Our aim here is to calculate the static shear and normal stress fields induced by a dislocation movement. To compute these quantities, we started from Dunbar's basic program DIS3D, which was updated by Erickson (1986) and modified in 1993 following the recommendations of Okada (1992). This program calculates the stress and strain field everywhere in the discretized space provided that we introduce the following input parameters for the rectangular dislocation: fault geometry (length and width of the dislocation) and position (coordinates of the centre of the dislocation), fault orientation (strike and dip angles) and slip vector (strike-slip, dip-slip and opening displacement across the dislocation). A point to mention is that the standard program considers a uniform slip vector everywhere on the fault surface. Since it may be a strongly simplified slip pattern, we have modified the initial model in order to enter more complex slip distributions. This is done by simply subdividing the fault into a network of many rectangular cells. A slip vector is then attributed to each cell. Since we have no limitation on the number of these cells, we can conveniently introduce various slip distributions. Usually, two simple slip models are considered as alternatives:

(1) a uniform slip along the fault, or
(2) an elliptic slip distribution along the fault.

This second model requires some explanations. Let us consider a Mode III crack on the $y' = 0$ plane, extending from $x' = -l$ to $x' = l$ along the X'-axis, and of infinite size along the Z'-axis. According to the 2-D elastic crack theory, the displacement U_s on the crack at a point x' along the X'-axis is related to the tangential stress drop $\Delta\tau$ through the analytical expression:

$$U_s(x') = \frac{2(1-\nu_u)\Delta\tau}{G}\sqrt{(l/2)^2 - x'^2} \tag{17}$$

where l is the length of the fault and $x' = 0$ corresponds to the centre of the fault. Thus, the stress drop is uniform as soon as we consider an elliptic slip distribution. Even though this is no longer strictly valid for a rectangular fault (i.e. of finite size along the Z'-axis), the second slip model is referred to in the following as the uniform stress-drop model.

Fig. 2(a) presents the uniform slip model (1) and a variable slip model (2) in the case of a pure strike-slip fault. The faults and their associated reference axes (X', Z') are represented as well as the strike component of slip U_s for the various cells. The different shades of gray on the cells of the mesh indicate the intensities of the slip vectors attributed to each cell. The slip vector for each individual cell i depends on its position x'_i along the fault. In the case of pure strike-slip, the dip component U_d is evidently zero everywhere. Since our fault slip model is discretized, the quality of the approximation of the analytical expression for the model with constant stress drop will depend on the number of mesh cells along the strike direction. More complex slip distributions $U_s(x'_i, z'_j)$ and $U_d(x'_i, z'_j)$ can also be easily introduced at the cell location (x'_i, z'_j). The stress/strain fields generated by the fault movement are then obtained by superimposing the contribution of each individual cell.

Fig. 2(b) gives a schematic representation of the fault model in its tectonic environment. The slip vector of one cell is represented with its strike and dip components, while the grey levels of the various cells correspond again to the various intensities of slip vectors for each cell. In this diagram we also represent the horizontal regional stress fields. These stresses must be superimposed onto the stress disturbance due to the seismic event in order to calculate the total stress field. In the following, the tectonic stress field is introduced in the simplest way. The deviatoric part of the background tectonic

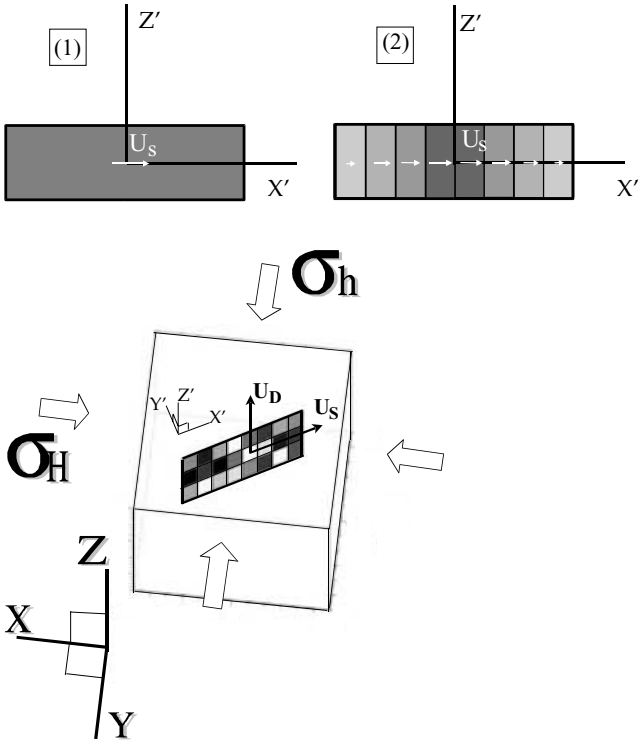

Figure 2. Top: Pure strike-slip faults in the reference plane (X', Z'): (1) uniform slip model; (2) variable slip model. The displacement on the fault is restricted to the strike component U_s, which is indicated by the white arrows. The various grey levels correspond to various intensities of the slip vectors for each cell. Bottom: Schematic view of the fault in its tectonic environment. The fault surface is subdivided into a rectangular network of cells each having its own slip vectors. The strike and dip components of slip for one cell are represented on the figure.

stress tensor is simply assumed to have the following form:

$$\sigma_{ij} = \begin{pmatrix} \sigma_H = -\sigma & 0 & 0 \\ 0 & \sigma_h = \sigma & \\ 0 & 0 & 0 \end{pmatrix}$$

in the case of a strike-slip fault and

$$\sigma_{ij} = \begin{pmatrix} \sigma_H = -\sigma & 0 & 0 \\ 0 & 0 & \\ 0 & 0 & \sigma_v = \sigma \end{pmatrix}$$

for a reverse fault.

The background tectonic deviatoric stresses are not allowed to vary with depth. Even though it is probably an unreasonable approximation, this simplification is made deliberately to avoid the introduction of additional variables. We note, however, that a knowledge of the regional stress field is not important as far as the stress perturbation resulting from the dislocation movement is concerned. Indeed, the stress disturbance as well as the stress drop associated with the event are determined as soon as the slip model is chosen. The relationship with the energy radiated by the earthquake is determined using the moment magnitude M_w, which depends directly on the geometrical characteristics of the fault and the slip model according to the formula $M_w = 2/3 \times log_{10}(M_0) - 10.7$, where the seismic moment M_0 is expressed in dyn cm^{-1} (Hanks & Kanamori 1979).

2.2.3 Rupture criterion and aftershock triggering

As seen previously, the proximity to failure at a given point following an earthquake may be analysed in terms of the Coulomb failure function (ΔCFF). All the results discussed below consider the optimal CFF criterion following the approach of Oppenheimer *et al.* (1988). The Coulomb failure function is expressed as:

$$\mathrm{CFF} = \tau_{\mathbf{n},\mathbf{t}} + \mu(\sigma_{\mathbf{n}} + P) \tag{18}$$

where **n** and **t** refer, respectively, to the unit vector normal to the fault plane and the tangential unit vector in the slip direction, both oriented to yield the maximum CFF value. $\tau_{\mathbf{n},\mathbf{t}}$ and $\sigma_{\mathbf{n}}$ are the corresponding shear and normal stresses. Implicitly, the optimal Coulomb failure function criterion assumes that faults exist in all orientations at each location around the main fault. By knowing the regional stress field we can define the initial CFF. Then we add the change in stress due to the earthquake and the regional stress field, which thus allows us to calculate the total stress field. We then look for the optimal direction of failure by considering the rotation of the principal stresses and calculate the CFF value for the optimally oriented plane of failure. As seen above, the background tectonic deviatoric stresses are not allowed to vary with depth. This probably has some effect on the value of ΔCFF. However, taking account of the depth dependence of the tectonic deviatoric stresses would probably not substantially modify the general applicability of our results.

As mentioned in Section 2, the CFF will increase in the dilated zones and decrease in the compressed area. Let us examine ΔCFF for the various attitudes of the fault plane, starting from the initial time of the main event $t = t_0$ up to the final time t_f (that is, the time to reach a totally relaxed state). In order to describe the failure, we need to make some assumptions about the mechanical strength of the faults in the main fault area. First of all, the rupture criterion should be consistent with the Coulomb stress concept. In this way, the mechanical resistance of a fault is fully described as soon as we know its residual shear strength and friction. At a given location, knowing these parameters and the orientation of the pre-existing faults, we should be able to predict where some failures might occur. The friction coefficient as well as the residual strength are likely to vary over a certain range of values. Usually, the static friction is found to be around 0.6–0.9 in the laboratory Byerlee (1979). However, the fault orientation in the field displays some evidence for a lower apparent friction Zoback *et al.* (1988). Although the fault residual strength is usually zero at low normal stress, it is likely to increase with normal stress as stated by Byerlee's law. It will also vary, for example, through fluid-assisted lithification processes within gouge zones. Finally, the fault orientation plays a major role, since the slip occurs on the best oriented plane. Depending on the fault orientation, the strength should cover a broad distribution. It is not our intention here to enter the debate on fault strength; but rather to introduce some reasonable and simple assumptions. A simple way to introduce a strength distribution is to consider that the friction coefficient is constant everywhere and to assign a distribution of residual strength to the defects around the main fault. Clearly, since the main fault slides first, its residual strength is lower than in the surroundings. In the following, the term 'residual strength' must be taken in a relative sense, referring to the residual strength of the main fault. Thus, we consider that the residual strength of the principal fault is zero and the phrase 'distribution of residual strength' incorporates all the complexity inherent in the definition of strength, i.e. possible variations in residual strength, friction and orientations of faults. It is important to know how many faults are present within

one discretized cell. We consider here that a large number of faults may exist (usually 128 within each block). Indeed, the statistics of the events are likely to be disturbed otherwise. As far as the temporal variation of aftershocks is concerned, we expect that a small number of faults within each cell would increase the variance of the number of events (assuming several runs). Therefore, we tested two distributions:

(1) A discrete distribution, whose residual strength varies between a minimum value $S_{\min}$, which is the minimum ΔCFF required for triggering aftershocks, and a maximum value, which is larger than the maximum ΔCFF reached in the entire volume, whatever the time. Between t and $t + dt$, and within a given volume, the number of aftershocks will be obtained by considering the number of faults having a residual strength comprised between CFF^t and $\mathrm{CFF}^{(t+dt)}$.

(2) An alternative approach would be to use a continuous distribution. In that case, the number of aftershocks would be directly proportional to $\mathrm{CFF}^{(t+dt)} - \mathrm{CFF}^t$ (assuming this value to be >0) and the distribution of residual strength does not need to be limited upwards. Thus, the residual strength is distributed between $[S_{\min}, \infty]$.

Both approaches provide similar results. The only difference is that the continuous distribution of residual strength provides an average value for the distribution of aftershocks, whereas in the discrete case the distribution of aftershocks will be dispersed around this average. To simplify, we consider here a constant distribution of residual strength over the interval of definition.

Finally, it is noteworthy that we do not consider the stress disturbance associated with the triggering of aftershocks. This is done deliberately to avoid time-consuming calculations. Taking into account the disturbance associated with large aftershocks would probably have a second-order effect on both the spatial and temporal distribution of aftershocks. Depending on the stress field generated by the aftershocks, the disturbance may either enhance or inhibit the number of aftershocks. This will be the object of a later study.

3 NUMERICAL SIMULATIONS

In the following, we consider several situations corresponding to various tectonic settings and fault geometries. The main parameters used in the models are summarized in Table 2.

3.1 Spatial distribution of aftershocks

3.1.1 The strike-slip case

Model 1: In the following we consider a fault making an angle of 25° with the maximum far-field principal stress σ_H, which is assumed to be in the X direction (see Fig. 3). The minimum principal stress σ_h lies in the Y direction. The fault is optimally oriented for a friction coefficient equal to 0.84. The fault length and width are set at 80 km and 20 km, respectively, i.e. representative of a major earthquake. Accordingly, the magnitude of the event is $M_w = 7.5$. This yields an average strike-slip vector U_S equal to 4.15 m. The fault movement is dextral and we assume $|\sigma_1 - \sigma_3| = 100$ MPa.

In Fig. 3(a), we show the change in pore pressure as a result of an earthquake event. In this case we assume an elliptic displacement and, consequently, a constant stress drop along the fault. The resulting pore pressure is shown in Fig. 3(a). We observe zones of increasing and decreasing pore pressure consistent with the focal mechanism of the earthquake. Fig. 3(b) displays the ΔCFF pattern respectively at $t = t_0$ on the left-hand side and at t_f on the right-hand side. At $t = t_0$ the zones where ΔCFF increases are located both in the areas of depressed pore pressure and in lobes situated in the continuity of the fault. The solid curves correspond to the contour curves for $\Delta\mathrm{CFF} = 0.1$ MPa and 0.5 MPa at $t = t_0$. However, since this pattern corresponds to an undrained situation, it has no meaning when the timescale is considered. At best, the possible fracturing associated with this positive Coulomb stress change may lead to co-seismic fracturing. Since it is triggered by the main fault it could be tempting to confuse this effect with aftershocks. However, since this fracturing is a co-seismic effect, we merely see the secondary fractures as a part of the complexity of the fault. Since these features are located at both edges of the fault, it is quite acceptable to assign them to some geometrical complexity at the edges. The situation is more complicated when the co-seismic fracturing occurs at a greater distance away from the immediate vicinity of the principal fault, in which case it cannot be considered as belonging to some fault complexity. Since ΔCFF is usually higher close to the fault, this situation is not very common (even though it depends on the value of ΔCFF considered as necessary for fracturing). As far as the distribution of residual strength is concerned, we consider here that $S_{\min} = 0.5$ MPa, with a uniform distribution of residual strength above this value. The value of $S_{\min} = 0.5$ MPa chosen prevents co-seismic fracturing away from the main fault.

Here, we are mainly interested in the spatial variation of the Coulomb stress with time. The ΔCFF curves on the right-hand side

Table 2. Table of the parameters used for fault geometry and tectonic setting in the various models.

Model parameters	Strike-slip			Reverse fault	Northridge event[a]
	Model 1	Model 2	Model 3		
Magnitude	7.5	7.5	7.5	7.5	6.7
Friction coefficient	0.84	0.268	0.84	0.84	0.4 Stein *et al.* (1994)
$\lvert\sigma_1 - \sigma_3\rvert$ (MPa)	100	10	100	100	10 Stein *et al.* (1994)
Length (km)	80	80	80	80	20
Width (km)	20	20	20	20	26
Fault strike	25°	37.5°	25°	90°	93° Stein *et al.* (1994)
Fault dip	90°	90°	90°	25°	41°
Slip pattern	Elliptic	Linear var.	Elliptic+ heter.	Elliptic	Variable slip
Strike-slip (m)	4.15	4.15	4.15	0	0.77 (positive rake 90°)
Dip slip (m)	0	0	0	4.15	−0.04 (positive rake 180°)

[a]From Hudnut *et al.* (1996).

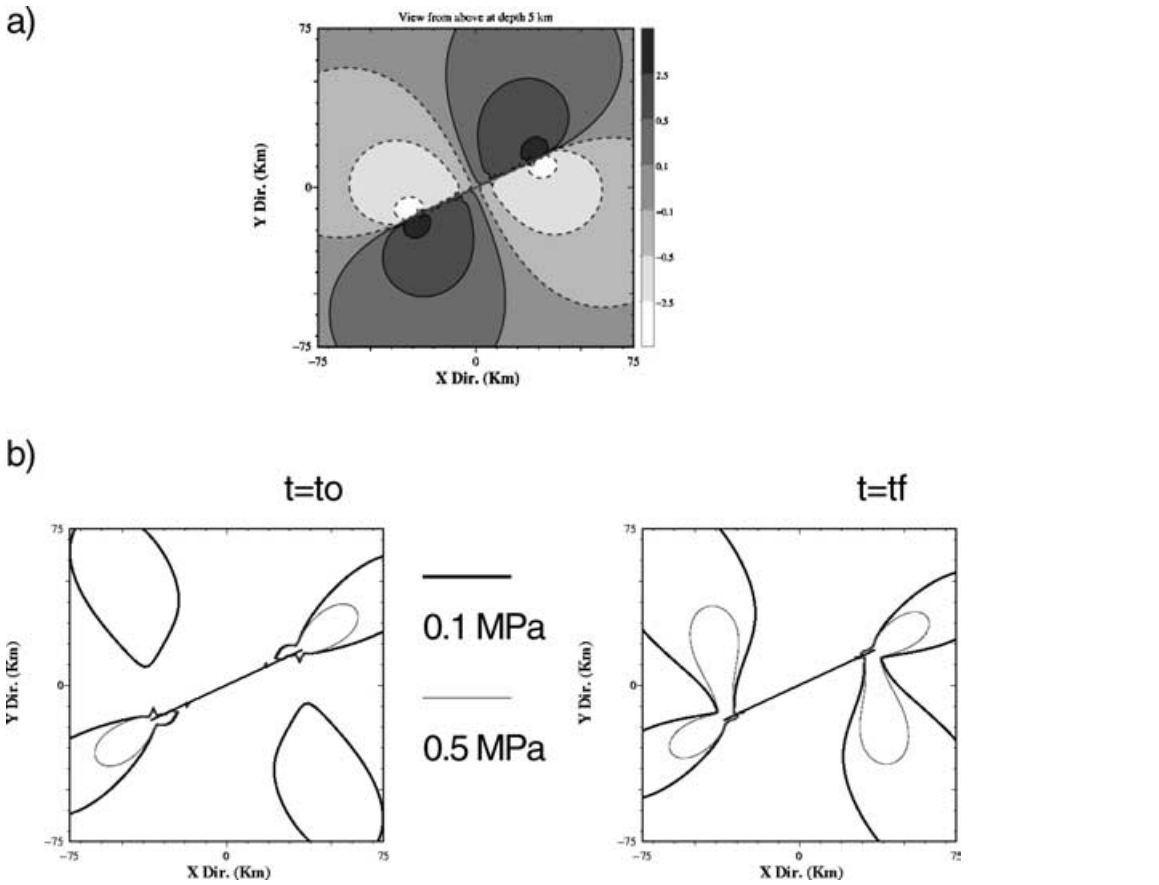

Figure 3. (a) Change in pore pressure due to a dextral strike-slip fault movement (in MPa). (b) ΔCFF resulting from the strike-slip movement. The grey curve and the black curve correspond, respectively, to the contour curves with ΔCFF = 0.5 MPa and ΔCFF = 0.1 MPa at t_0 (i.e. for undrained conditions) on the left-hand side and at t_f (i.e. when fluid pressure is completely relaxed) on the right-hand side. The zones delimited by the iso-ΔCFF values expand with time at locations recording a pore pressure decrease at $t = t_0$ and a consecutive increase of fluid pressure with time.

of Fig. 3(b) correspond to the same contour curves as previously (ΔCFF = 0.1 MPa and 0.5 MPa), but for $t = t_f$ (i.e. at the time of complete pore- pressure relaxation). Let us consider, for instance, the isovalues ΔCFF = 0.1 MPa. We observe that the zone expands with time in the dilated area. This is due to the increase of post-seismic pore pressure in this area following the main shock. The co-seismic lobe on the side of the fault tip with ΔCFF = 0.5 MPa has a very limited extent (see Fig. 3b). Thus, in order to explain the occurrence of aftershocks on the side of the fault tip a smaller S_{min} would be required if we only consider the co-seismic effect. In other words, co-seismic analysis would lead to an underestimation of the ΔCFF value required for aftershocks to be triggered. As a consequence, the poroelastic approach is likely to provide results that differ widely from an analysis based on an undrained ΔCFF approach. Introducing a distribution of residual strength makes it possible to analyse the distribution of aftershocks.

Considering the distribution of strength around the main fault, we are able to simulate the occurrence of aftershocks. This is illustrated in Fig. 4. The various dots correspond to the aftershocks in the 3-D volume (the various symbols indicate different event times), projected onto the plane at a depth of 5 km. Only a few events occur in continuity with the main fault, whereas the analyses based on static Coulomb stress would consider the zones of co-seismic increase at the tip of the fault as potential sites for aftershocks. In Fig. 4 , we report the aftershocks after $t_2 = 2\Delta t$ (blacks dots), $t_5 = 5\Delta t$ (grey dots) and $t_{100} = 100\Delta t$ (open square), where Δt is a reference time step. At short time values $2\Delta t$ and $t = 5\Delta t$, we observe after-

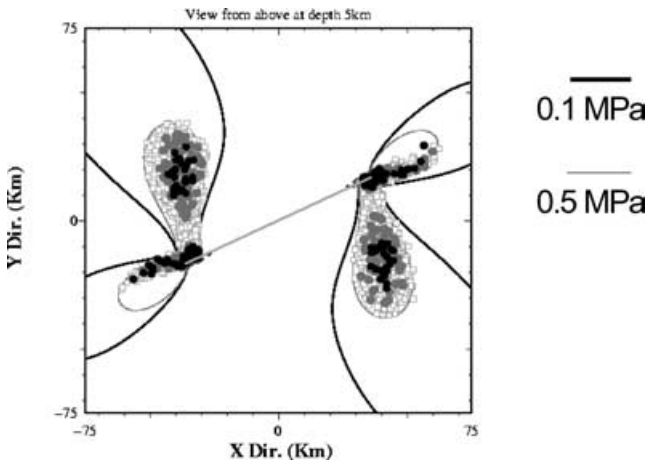

Figure 4. Spatial distribution of aftershocks derived from the strike-slip model 1 (elliptic slip model, $\mu = 0.84$, strike angle = 25°, $|\sigma_1 - \sigma_3| =$ 100 MPa) at various time steps. The black dots, grey dots and white squares correspond, respectively, to $t = 2$ days, $t = 5$ days and $t = 100$ days.

shocks at the same time located close to the tip as well as off the fault. This kind of aftershock pattern can be observed, in particular for the Landers earthquake, and, as noticed by Li *et al.* (1987), it appears that aftershocks may occur both close to the fault and off the fault. At longer timescales, aftershocks diffuse between both of these locations. This means that although the driving mechanism is

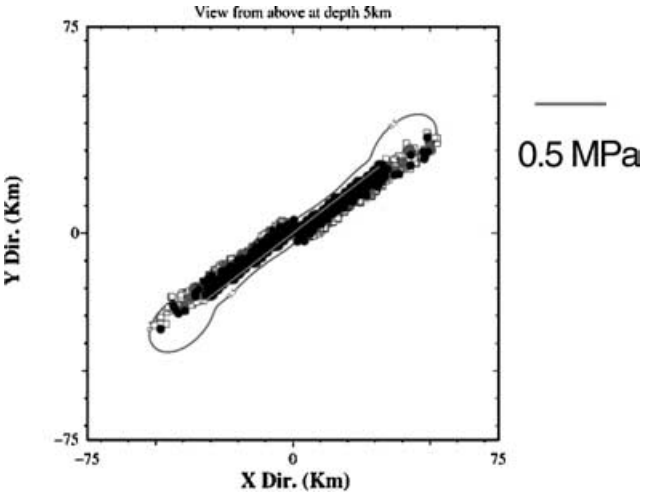

Figure 5. Spatial distribution of aftershocks for the strike-slip model 2, when changing the friction coefficient and the associated fault direction as well as the slip distribution (linearly variable slip model, $\mu = 0.268$, strike angle = 37.5°, $|\sigma_1 - \sigma_3|$ = 10 MPa).

controlled by fluid diffusion the shape of the diffusion front is complex and requires a perfect knowledge of the co-seismic Coulomb stress pattern. Since it depends on the slip geometry as well as the fault geometry and the tectonic stress field, we need to have good control of all of these parameters.

While there are many examples of aftershock concentrations at the fault edge, another noticeable feature of this simulation is that it does not predict aftershocks along the fault, as usually observed in seismological data for strike-slip faults. However, many researchers indicate zones of high ΔCFF along the fault. The question here is whether fluid weakening can lead to triggering of aftershocks along the fault or whether another mechanism should be invoked.

Model 2: In order to allow the appearance of aftershocks along the fault, we consider here another situation described in Table 2. $|\sigma_1 - \sigma_3|$ is set at 10 MPa and we assume a fault strike of 37.5°. Since once again we consider the best oriented fault, the friction coefficient is chosen accordingly as $\mu = 0.268$. The fault length and width are similar to the values chosen in model 1 (see Table 2). We consider that the magnitude of the slip increases linearly from zero at the edge of the fault to a maximum value at the middle of the fault. Using these parameters, we simulate the aftershock distribution in a similar manner to the previous case. Results are shown in Fig. 5. According to this figure, aftershocks may indeed be triggered along the fault. The main point here is that the stress induced by the slip close to the fault should be comparable to the tectonic stress. Large positive ΔCFF values along the main fault may be found, by using the maximum CFF criterion. Indeed, lowering $|\sigma_1 - \sigma_3|$ is likely to induce a rotation of the principal stress axes, consequently changing the orientation of the planes that are optimally oriented for sliding. The positive ΔCFF along the fault is a direct consequence of this modification. Lowering the friction coefficient has a minor effect, and aftershocks still occur along the fault even if the friction coefficient in the surroundings of the fault (for instance $\mu = 0.84$, as previously) differs from the apparent friction $\mu = 0.268$ responsible for the orientation of the main fault. In addition, using $|\sigma_1 - \sigma_3| =$ 10 MPa in model 1 would yield aftershocks along the fault, but, in this case, they are less numerous. In the present case we notice that although aftershocks are distributed along the fault, the distribution is slightly asymmetric in agreement with the distribution of volumetric change. We should mention, however, that this mechanism occurs under particular (although not unrealistic) conditions. Nevertheless, increasing $|\sigma_1 - \sigma_3|$ would prevent the appearance of aftershocks along the fault.

Model 3: We start from the same configuration as used for the simulation of Fig. 4. The only parameter that is allowed to change is the distribution of slip. The fault is discretized with a mesh size of 4000 m × 4000 m. The distribution of slip deviates randomly from that of model 1, in regard to both the strike and the dip directions. Within each cell, the amplitude of the deviation at its maximum amounts to 20 per cent of the initial slip amplitude. The slip vectors are displayed in Fig. 5(b). Comparing the aftershock distribution with Fig. 4, we indeed observe that the aftershocks are allowed to occur along the fault plane (see Fig. 5a). They are not uniformly distributed and may be lacking in some places. We attempt to show here that the fluid flow may provide a mechanism for triggering the aftershocks along the fault plane in relation to the slip distribution. As noticed by Bakun *et al.* (1986), the aftershocks seem to occur at the periphery of the slip. However, a thorough analysis of the aftershock pattern in relation to the slip distribution would lie outside the scope of this paper.

3.1.2 The reverse fault case

The main objective here is to compare the predictions for strike-slip and reverse faults. The difference in fault movement geometry is likely to yield a distinctly different compression/dilation pattern, and thus modify the distribution of aftershocks. We simulate a reverse fault using a friction coefficient equal to the value used in model 1. The fault dip is chosen accordingly as equal to 25°. The down-dip distance to the upper fault edge is 5 km and the fault width is 20 km. In Fig. 7(a), we report the change in pore pressure resulting from the movement of the fault. We observe a relatively large zone of co-seismic decrease in pore pressure. In Fig. 7(b), we plot the ΔCFF = 0.5 MPa contour curves at t_0 and t_f. Using this model, we simulate the occurrence of aftershocks in Fig. 8, again assuming $S_{min} = 0.5$ MPa. The main feature apparent on the cross-section is that the aftershock distribution is more diffuse than in the case of strike-slip. Therefore, aftershocks cannot be used to define the fault plane, which is consistent with most of the observations. In addition, we note that the volume affected by the presence of aftershocks increases with time away from the fault area. However, it may appear paradoxical to predict this result in view of the ΔCFF stress distribution at the undrained and the relaxed states in Fig. 7(b) together with the change in pore pressure (Fig. 7a). Indeed, we sometimes observe ΔCFF values higher than 0.5 MPa just after the earthquake at some localities, whereas late aftershocks occur in such zones. Since the change in fluid pressure is negative, we might expect early aftershocks in these areas due to the relaxation of fluid pressure. However, according to Fig. 7(a), there is a strong fluid pressure gradient toward the tips of the fault. In areas where late aftershocks occur, the fluid pressure starts to decrease due to this pressure gradient and then increases up to the relaxed state. This particular behaviour explains why the aftershocks are delayed in these zones. The complexity of the geometry of the change in fluid pressure, which depends on the geometry of the fault and on the slip pattern, may lead to a wide variety of behaviours.

3.2 Time distribution of aftershocks

3.2.1 Predicted decay laws using the model

As seen above, the time dependence of the aftershock distribution is well known and has received much attention for a long time. In this

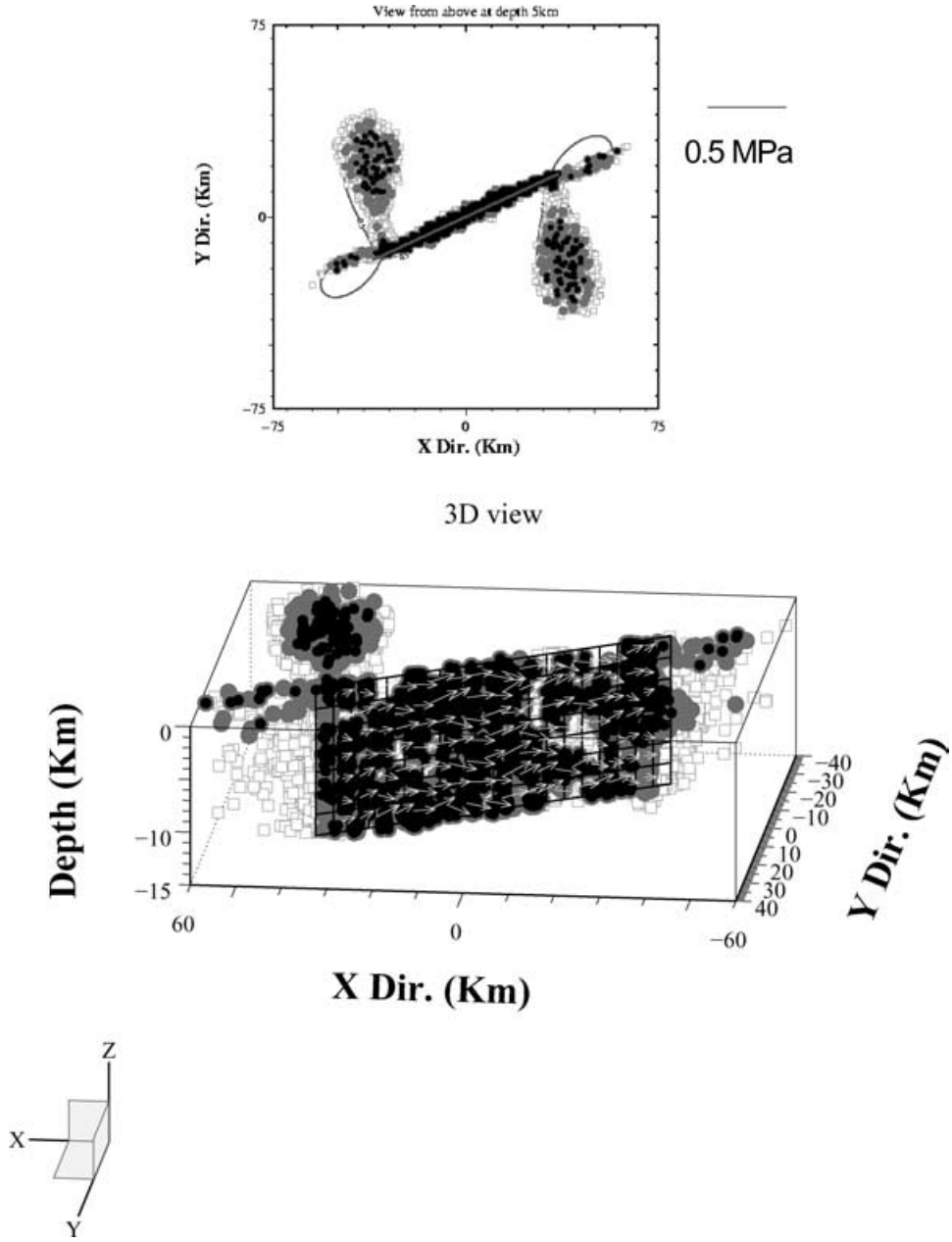

Figure 6. Top: Plan view of the spatial distribution of aftershocks for the strike-slip model 3 (elliptic slip model + randomly variable slip component, $\mu = 0.84$, strike angle = 25°, $|\sigma_1 - \sigma_3| = 100$ MPa). Bottom: Spatial distribution of aftershocks (3-D view). The discrepancy with the slip model 1 is represented by the arrows on the discretized mesh cells of the fault.

section, we aim to investigate the temporal response derived from the model. As pointed out by Nur & Booker (1971), a 2-D fluid flow leads to an Omori coefficient equal to 0.5. The time dependence of aftershocks can be calculated by assuming that aftershocks may occur everywhere in the dilated area. This has led Nur & Booker (1971) to calculate the rate of aftershock occurrence as:

$$n(t) = \partial N(t)/\partial t \propto \int_V (\partial P/\partial t) dV \tag{19}$$

where $N(t)$ is the cumulative number of aftershocks and V is the integration volume, i.e. the volume within which pore pressure P is increasing. However, contrary to the suggestion of Nur & Booker (1971), the integration volume is finite and varies with time, so the integration in eq. (19) must be performed numerically. Starting from a dimensional analysis, the time dependence of the aftershocks can be written as:

$$n(t) \propto N_f\, l_c^3 \frac{1}{\tau} F(t/\tau) \tag{20}$$

where N_f is the density of defects per unit volume and τ is the time constant of relaxation associated with the diffusion process. It can be expressed by $\tau = l_c^2/c_m$, where c_m is the diffusion coefficient and l_c is the characteristic distance of diffusion. l_c scales proportionally to the fault slip d and is related to the size of the static lobes. For convenience, we consider here that $l_c = d\ (1 \times 10^4)$ (implicitly, this assumes that, for a ratio $d/l = 2.5 \times 10^{-5}$, l_c should be around $l/4$.

In order to calculate the time dependence of aftershock decay, we start from the strike-slip model 1 and use the continuous distribution

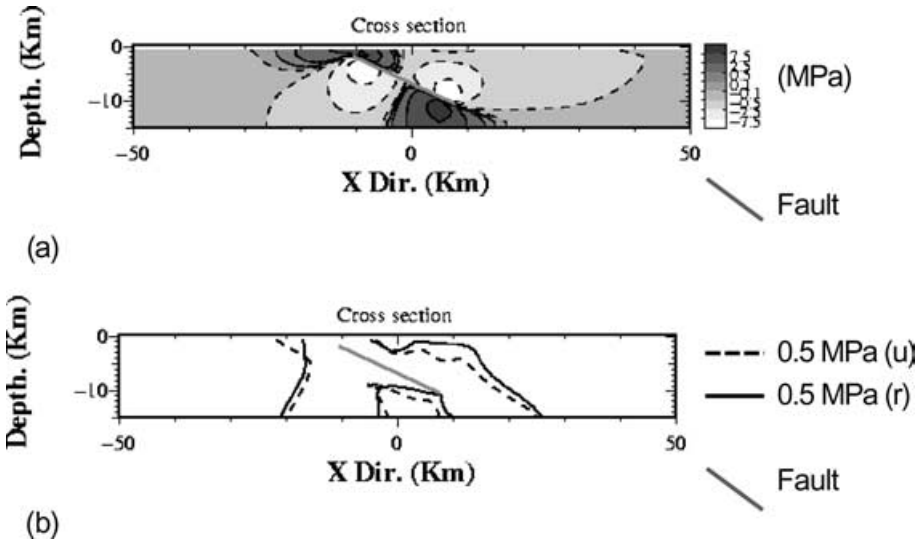

Figure 7. (a) Cross-section showing the change in co-seismic fluid pressure for the reverse fault model of Table 1 (elliptic slip model, $\mu = 0.84$, dip angle = 25 ○, $|\sigma_1 - \sigma_3| = 100$ MPa). (b) ΔCFF in the undrained state $t = t_0$ (dashed curve) and in the relaxed state $t = t_f$ (solid curve).

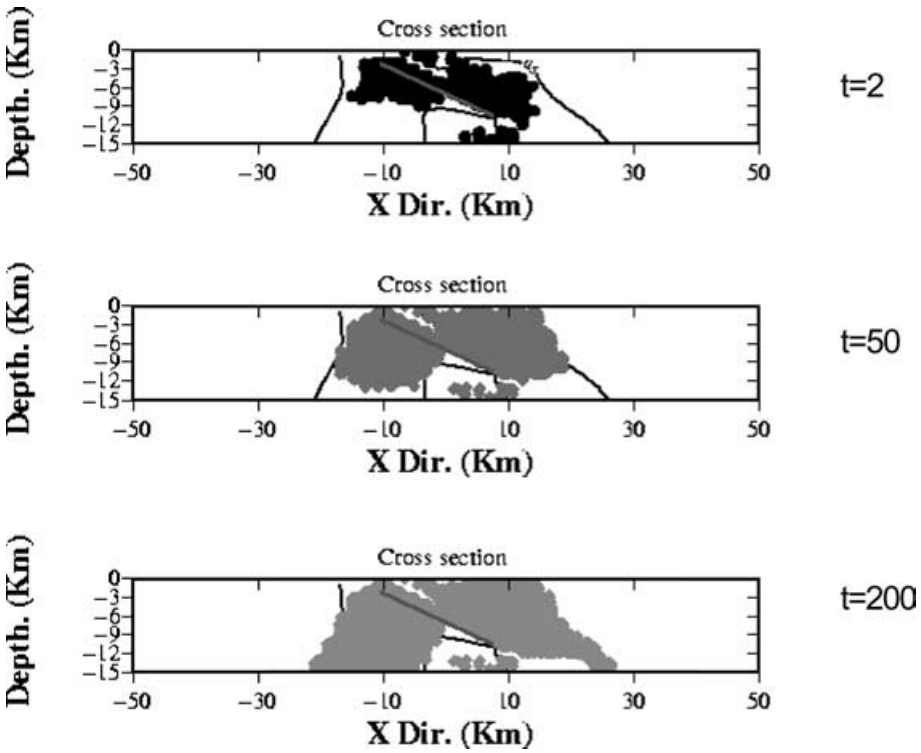

Figure 8. Spatial distribution of aftershocks at $t = 0$ days, $t = 50$ days, $t = 200$ days for the reverse fault model of Table 1.

of residual strength to calculate the number of aftershocks per time unit. $F(t^* = t/\tau)$ accounts for the time dependence of aftershocks. In Fig. 9, we use a log–log plot to show the shape of the normalized function for the strike-slip case. This function can be conveniently fitted using a function of the form

$$F(t^*) = K_0/(c^* + t^*)^r e^{-\alpha t^*}. \quad (21)$$

Using a least-squares non-linear fit we calculate the parameters c^*, α and r for both the reverse fault and the strike-slip cases. Both functions have similar shapes. The results are given in Table 3. The shape of this function allows us to discuss the time dependence of the aftershock distributions in the following terms:

(i) For $t^* \ll t_a^* = 1/\alpha$, the function F displays a behaviour that is close to the Omori law (see eq. 1). The value of c is given by $c^*\tau$. But are these values comparable with seismological data? Using the parameters of model 1 (see Table 2), we find that $c \approx 1$ for a permeability $k \approx 2 \times 10^{-15}$ m^2. This means that c should be around 0.1 for a value of $\approx 2 \times 10^{-14}$ m^2, and around 10 for $k \approx 2 \times 10^{-16}$ m^2. This may be compared, for example, with the values given

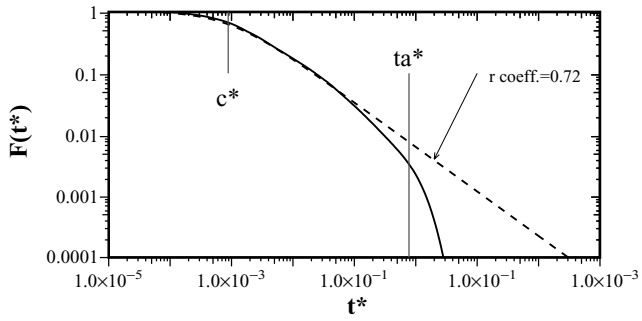

Figure 9. Normalized function $F(t^*)$ of decay in number of aftershocks for a strike-slip model. c^* is the normalized value of c in eq. (21) and $t_a^* = 1/\alpha$ is the time to attain the exponential regime.

Table 3. Parameters derived from the decay law (eq. 21).

Parameters	Strike slip	Reverse fault
c^*	$(8.82 \pm 0.08) \times 10^{-4}$	$(1.03 \pm 0.008) \times 10^{-3}$
α	1.29 ± 0.05	1.69 ± 0.04
r	$(0.72 \pm 2.0) \times 10^{-3}$	$(0.62 \pm 1.6) \times 10^{-3}$

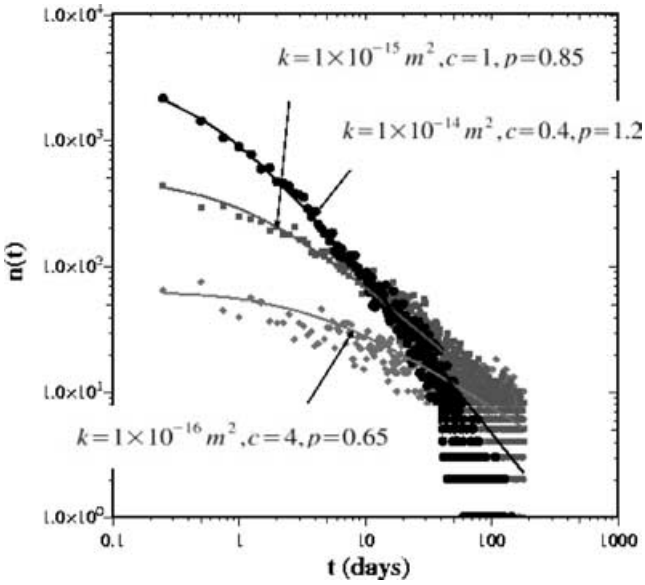

Figure 10. Number of aftershocks with time for various values of K. The various solid curves correspond to the fit of the Omori law (eq. 1) using the derived Omori parameters.

by Ogata (1989) and Ogata (1992), which are usually less than 1 (a few hours), but which have been found to vary between 0.001 and 11.6. We also note that the c^* value derived in our simulations is expected to depend on the discretized mesh size. Smaller blocks lead to a smaller c^* value. Since it is influenced by the exponential term, the function F on a log–log plot displays a behaviour that remains relatively close to the Omori law, with an 'apparent' p coefficient higher than r. Starting from the function F, we derive the value $p \approx 0.75$ in the 'power-law' domain, using a non-linear fit. We notice, however, that the decay law deviates slightly from the pure Omori behaviour for t^* values close to $t_a^* = 1/\alpha$.

(ii) For $t^* > t_a^* = 1/\alpha$, the function F is dominated by the exponential term and no longer matches the Omori law. Considering a permeability $k \approx 2 \times 10^{-15}$ m^2 (i.e. the value of k required to obtain a value of $c \approx 1$) and using the parameters of model 1, we expect to reach the exponential regime for $t \approx 900$ days. This value would be reduced to 90 days when $c \approx 0.1$ (i.e. for $k \approx 2 \times 10^{-14}$ m^2).

Let us compare these results with the parameters derived from the seismological data. The modified Omori law is routinely used in seismology and, in spite of some deviations, has been found to describe the data satisfactorily. However, Kisslinger (1993) and Gross & Kisslinger (1994) present an alternative decay function called the stretched exponential function, which can be expressed as:

$$N(t) = K_0 t^{q-1} e^{-qt/t_0}. \tag{22}$$

Even though the exponential term has some influence, this is strongly limited by the q exponent in the exponential term. Indeed, Kisslinger (1993) found that q varies between 0.3 and 0.5. As a consequence, the exponential decay for $t^* > 1/\alpha$ cannot be accounted for using a stretched exponential function, unless we consider t_0 is much lower than the values derived by Kisslinger (1993). We suggest that, at least for a certain range of permeability values, τ/α can be taken as equivalent at characteristic time t_a, as introduced by Dieterich (1994), describing the return of seismicity to a steady state. Thus, for 10^{-14} m^2 $< k < 10^{-15}$ m^2, we expect the decay to follow an Omori-type law with an Omori coefficient $p \approx 0.75$ and a characteristic time t_a of between 100 and 1000 days.

For higher permeabilities, for instance at $k \approx 10^{-13}$ m^2, the decay occurs mostly in the exponential regime. Even though it does not follow the Omori law, the variation can be expressed as a power law over a limited range of time for which an apparent Omori coefficient can be derived. In order to provide a more concrete view of these ideas, starting from the reverse fault case, we simulate the aftershock time dependence for various values of hydraulic diffusivity (i.e. various values of τ). We performed simulations using the reverse fault model (see Table 2) for various values of permeability, taking the discretized distribution for modelling the residual strength. We allowed permeability to vary over two orders of magnitude from 10^{-16} m^2 to 10^{-14} m^2. For each simulation, we report the values of parameters for the Omori decay law. These values are reported in Fig. 10, for the three values of permeability chosen. The time step for counting aftershocks is 6 hr, and we report 6 months of aftershock decay. The results so obtained are consistent with those derived from Fig. 9 and allow a more direct comparison with the seismological data. As we pointed out previously, the Omori exponent increases with permeability, varying from 0.65 to 1.2 in the investigated domain of permeability. Notice that, since the Omori law does not include an exponent term, the variation of the c coefficient does not exactly follow the relationship $c = c^*\tau$. However, c increases with decreasing k. For values of k around 10^{-14} m^2, we observe that the temporal dependence deviates from the Omori law when the time is more than 1 or 2 months.

Finally, we need to stress that the decay law will be strongly dependent on the value of permeability. Spatial variations of permeability are likely to change the parameters of the derived Omori law. Moreover, we do not take into account the perturbations of the stress field associated with each aftershock and the resulting secondary aftershock sequences. This may have an effect on both the spatial and the temporal dependence of the aftershocks.

3.2.2 Application to the 1994 Northridge earthquake

To make further tests on this model, we attempted to model the time dependence of the 1994 Northridge earthquake. We used the

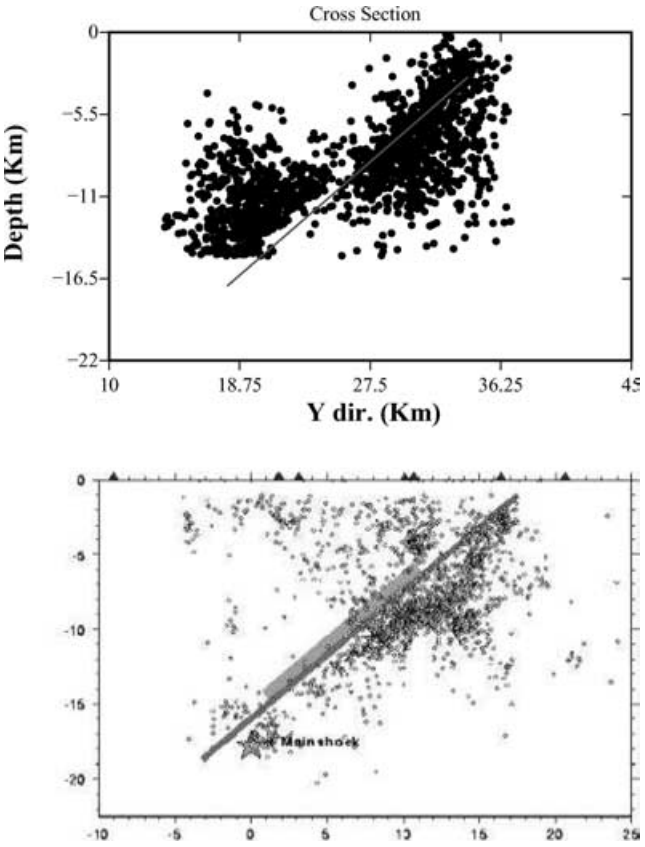

Figure 11. (a) Spatial distribution of aftershocks (cross-section) resulting from our modelling of the 1994 Northridge event using the slip model of Hudnut *et al.* (1996) (see parameters in Table 1). (b) Spatial distribution of aftershocks (after Hudnut *et al.* 1996).

model of Hudnut *et al.* (1996), which provides discrete values of the slip on a discretized mesh network of the fault and which has been inverted from GPS measurements. The lower threshold for aftershock triggering $S_{\min}$ is set at 0.5 MPa. As suggested by Stein *et al.* (1994), $|\sigma_1 - \sigma_3|$ is set at 10 MPa. The pressure dependence of the porosity is such that the Skempton coefficient is 0.4. Since the tectonic information is rather limited, we expect only a rough estimation of the spatial distribution of aftershocks. But it is sufficient as far as our present purpose is concerned. We attempted to calculate the time dependence of the aftershock distributions by using various initial guesses for the permeability. The final value chosen in this way matches reasonably well with the data provided by the National Earthquake Information Center of the USGS. The resulting spatial distribution of aftershocks is given in Fig. 11(a). This shows that our model provides a spatial distribution roughly in agreement with reality (Fig. 11b). We do not focus on the details here since the important point to discuss is the required value of permeability. Note, however, that the model does not satisfactorily predict the distribution of aftershocks in the lower part of the hangingwall. Even though this could merely be the result of the over-simplifications of the model, it may also be due to the disappearance of permeability at deep depths. Evidently, the problem requires more detailed information on the local geological features, but we do not think that this would significantly influence the time dependence of aftershocks. The value best fitting the aftershock data is $k = 7.5 \times 10^{-15}$ m^2. The results are shown in Fig. 12, and we observe that the temporal behaviour is relatively well modelled using these values. Finally, a

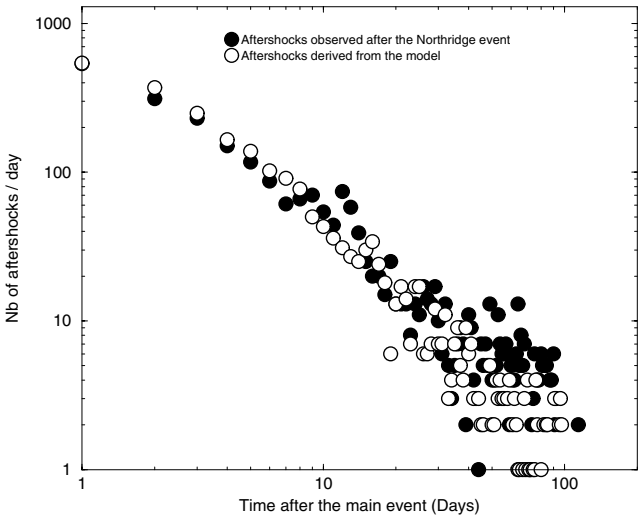

Figure 12. Comparison between decay in number of aftershocks for the 1994 Northridge event and present model using $k = 7.5 \times 10^{-15}$ m^2.

permeability of $K = 7.5 \times 10^{-15}$ m^2 may be considered as a fair over-estimate, being of the same order of magnitude as the value used in the modelling of Bosl & Nur (2002). We discuss this matter further below.

4 DISCUSSION

As mentioned above, we can see that the fluid flow may provide a mechanism for the triggering of aftershocks. Fluid flow represents an attractive mechanism, even though its effects should still be compared with the field data. Indirect studies of fluid relaxation processes Peltzer *et al.* (1998) as well as direct observations Muir-Wood & King (1987) provide some convincing evidence of fluid flow at crustal scales, yielding time constants that may be comparable with those of aftershocks. As already pointed out, if fluid is likely to flow with such a time constant, its mechanical effect should be taken into account. On the other hand, to improve our understanding of this phenomenon it is important to determine the implications on the structure of crustal permeability around the faults. According to the previous section, the permeability that matches best with the Northridge aftershock time decay is found to be around 7.5×10^{-15} m^2.

The first question related to the above discussion is: can this value be seen as representative of the permeability in a fault zone? Unfortunately, very little is known about permeability in fault zones. According to Davison & Kozak (1988), the values should range between 1×10^{-11} and 1×10^{-17} m^2. As a consequence, even though the required value for the Northridge event is within this range, the range is too large to allow us to draw a conclusion. A second point concerning the hydraulic properties in such areas is that of scale. Up to now we have only considered strong earthquakes and, consequently, this involves decametre- to kilometre-scale faults. The question that arises is: how does the model behave with varying scale length? Let us first consider a fault of length l and width $W \propto l$, with a slip of d. Let us apply a tenfold reduction in the fault dimensions ($l' = l/10$), as well as the slip vector ($d' = d/10$). In that case, the magnitude $M_{\rm w}$ decreases by two units: $M'_{\rm w} = M_{\rm w} - 2$. Since the ratio l'/d' is kept constant, the stress drop is constant and thus the Coulomb stress pattern can be obtained from the initial distribution by applying a scale reduction of 1/10. As far as the characteristic time is considered, we can write $\tau_c{}' = l'^2_c/c'_m = l^2/100/c'_m$. In order

to keep a constant time dependence of aftershocks, we need to impose the condition $c'_m = c_m/100$. In other words, the permeability should scale in the same way as L^2 (where L is the scale length) and M_w in order to maintain the same decay law at every scale. In the Omori law given by eq. (1), neither the exponent p nor the coefficient c have been found to vary with the size of the earthquake, so thus we require a spatial dependence of permeability. For a length scale of 60 km typical of a magnitude 7 earthquake, the permeability should be four orders of magnitude higher than for a length scale of 600 m, which may be representative of a magnitude 3 seismic event. The question is to know if such a type of scale dependence can be observed in nature. Scale-dependent effects are known to occur in the Earth's crust. Although measurements are still very sparse, Clauser (1992) provided a compilation of data for crystalline rocks showing that the permeability increases on average by around three orders of magnitude from laboratory scale (cm) to borehole scale ($\propto$100 m). At larger scales, the permeability seems to converge toward a homogenized value. Nevertheless, these data should be compared with the data compiled by Neuman (1994) based on dispersivity. According to these data, the variance of the permeability distribution increases with scale and follows a power law of the form $L^{0.5}$. According to Neuman (1994), the permeability in a 3-D model should vary as $k \propto \exp(L^{0.5}/6)$. Although Gavrilenko & Guéguen (1998) attempted to reconcile the points of view of Clauser (1992) and Neuman (1994), both sets of data remain rather contradictory according to their multiscale modelling. Finally we note that the permeability scaling behaviour in the neighbourhood of active faults remains mostly unknown. Although it is a speculative point of view, the L^2 scaling dependence cannot be ruled out by the data. Another viewpoint is to consider that indeed the representative elementary volume for fluid flow in the crust is reached at scale around 100 m. Brace (1980) provided values around (10–100)$\times 10^{-15}$ m^2 using processes involving fluid diffusion in the crust. These values are comparable to those given by Clauser (1992). If we accept that these values are representative of the crustal permeability above around 100 m, it is interesting to consider the consequences for the aftershocks. Such permeability values would provide a decay law for the time dependence of aftershocks consistent with values expected for an earthquake of magnitude around 7. In other words, according to our calculations the mechanical effect of fluids in the crust needs to be taken into account for this type of event. Even though this effect may not be the only mechanism, the order of magnitude of the fluid relaxation effect on the Coulomb stress indicates that it is a relevant mechanism for producing aftershocks. It is then an open question to know which mechanism takes over for seismic events of larger or smaller magnitude, while maintaining a similar Omori law. Even though they do not discuss the scale effect, Bosl & Nur (2002) provide convincing evidence that fluids may explain the spatiotemporal distribution of aftershocks for the Landers earthquake using a permeability around 1×10^{-15} m^2. However, from a more general point of view, since fluids involve a diffusive process, we need to know whether the expansion of the aftershock zone observed in real sequences is comparable with the model. Independently of the complexity of the shape of the diffusion front, the aftershocks generated by fluid-assisted processes follow a Brownian diffusion law. This has led Noir *et al.* (1997) to consider the possible effect of fluids in triggering the earthquake migration in the 1989 Afar seismic crisis. However, the inferred diffusivity is so large (i.e. 1×10^{10} m^2 s^{-1}) that unrealistic values of permeability would be required. As far as the 1992 Landers earthquake is concerned, Marsan *et al.* (2000) proposed a diffusion law of the form $R \propto t^H$ with H around 0.2. Marsan *et al.* (2000) indicate that this low exponent could be due to a subcritical fluid diffusion related to the heterogeneous fluid flow network. Nevertheless, the value of the diffusion exponent is strongly questioned in Chapter 9 of Helmstetter (2002), who found that the H value given by Marsan *et al.* (2000) is biased by the background seismicity. Helmstetter (2002) derived $H \approx 0$, which would indicate that there is no diffusion of aftershock activity. This measurement seems to contradict the results of Bosl & Nur (2002) as well as our present modelling.

Another aspect that deserves discussion concerns the hydrological signature of earthquakes. Peltzer *et al.* (1998) strongly suggested there is a link between the time constant for post-seismic fluid flow and the mechanical post-seismic effect. The question is whether these fluid flows can be observed through hydrological measurements. Muir-Wood & King (1987) provide a preliminary answer to this point. Indeed, the observed anomalies seem to be directly related to the focal mechanism. The interesting point here is to check whether these observations can be linked to the aftershocks. In Fig. 13, we plot the excess fluid flow expected following the Northridge event, using the parameters used in the previous section. In the central figure we map the peak excess flow that should result from these parameters. Since we are considering the peak flow, the corresponding time may change from one discretization node to another. Furthermore, it is noteworthy that the peak flow is positive in some places but, after a while, the fluid flow becomes negative. As a consequence, mapping the cumulative excess flow would give quite a different image of the spatial distribution of the excess fluid flow. Lastly, the excess fluid flow is expressed in mm day^{-1}, so the order of magnitude could be compared with the infiltrated rainfall per unit area. As we can see in Fig. 13, the order of magnitude of the excess peak flow close to the fault is around 0.1 mm day^{-1}, which is comparable to the observations reported by Muir-Wood & King (1987) in many cases. Assuming a volumetric discharge in the rivers of the area in question of around 10 l s^{-1} km^{-2} of hydrological catchment (this is the order of magnitude provided by Muir-Wood & King (1987)), a excess fluid flow of 0.1 mm day^{-1} would be easily detectable. Thus, the observations made by Muir-Wood & King (1987) seem to agree rather well with a hydrodynamic control of the temporal distribution of aftershocks. However, it is clear that the temporal variations of excess fluid flow should be convoluted with the transfer functions between the rainfall infiltration and the volumetric discharge within the rivers (or the water level change in wells) in order to compare the models with hydrological observations.

5 CONCLUSION

The main results of this paper are:

(1) Fluid flow following earthquakes provides an efficient time-dependent mechanism for triggering aftershocks. We model the aftershocks, both on the fault plane and off-fault, in terms of the attitude of the fault plane and its tectonic relations. The time dependence of the Coulomb stress may explain the limited success of predicting the spatial distribution of aftershocks using the co-seismic Coulomb stress pattern.

(2) We find that the Omori law can be derived from our model. However, the temporal dependence of aftershocks is strongly dependent on the permeability. This has important consequences for the permeability in the fault area. In particular, to ensure scale independence of the Omori law, the permeability should be scaled as L^2. Thus, even though fluid diffusion is a significant mechanism for aftershocks, we can still ask whether this mechanism is relevant at all scales.

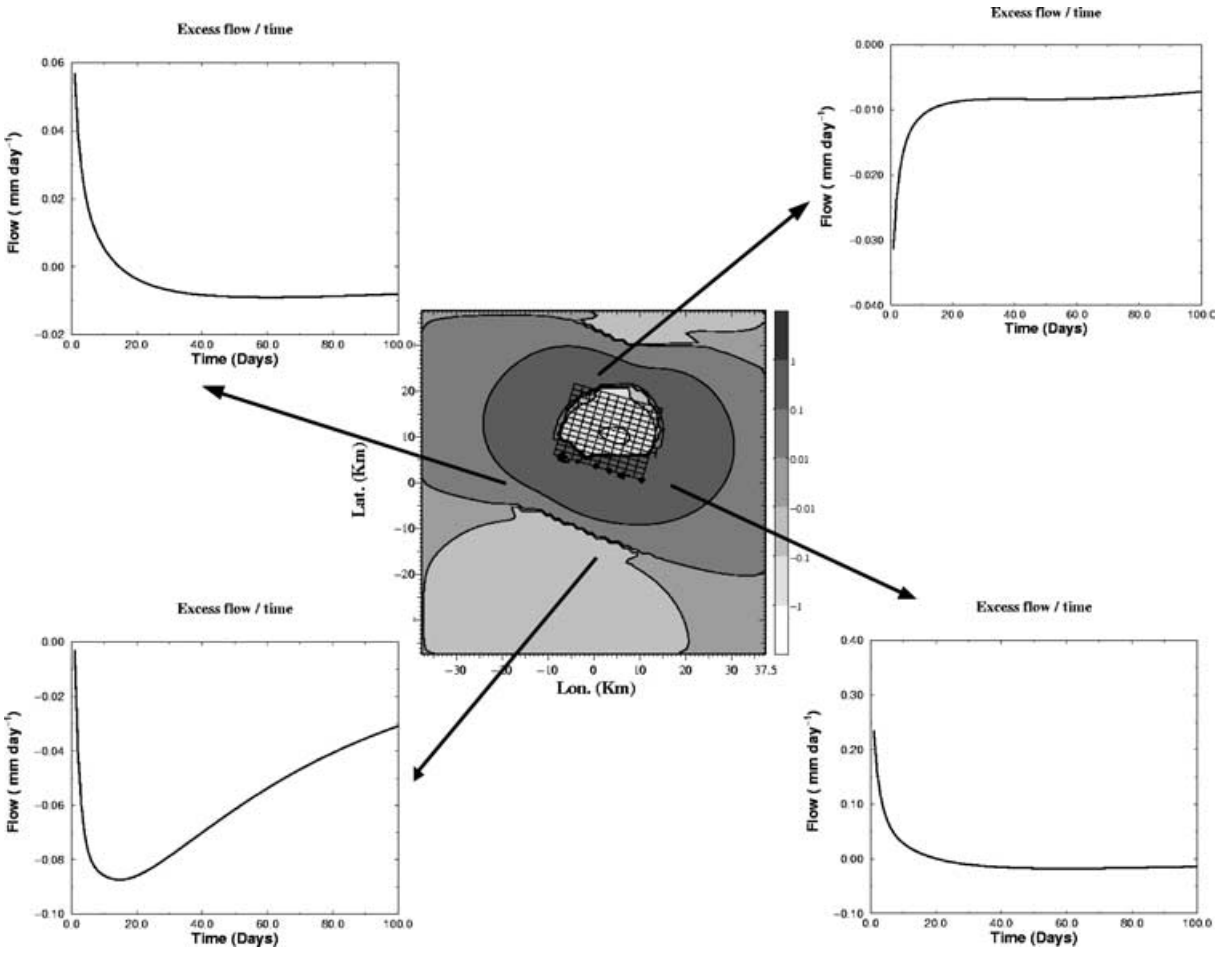

Figure 13. Map of the excess fluid flow following the Northridge event (assuming $k = 7.5 \times 10^{-15}$ m^2). The central image displays the peak of fluid flow (in mm day^{-1}), whereas the surrounding figures show the variations of excess fluid flow with the time for various locations around the fault.

(3) The Northridge post-seismic effect is modelled here, allowing us to derive a crustal permeability of around 7.5×10^{-15} m^2. The fluid flow associated with the occurrence of earthquakes should provide an observable hydrological signal.

ACKNOWLEDGMENTS

This work greatly benefited from discussions during the various stages of its development with S. Pride, my former colleague at Geosciences Rennes. I also wish to thank F. Cornet and P. Bernard for their very helpful comments. The idea about the relationship between fluid flow and aftershocks was initiated a long time ago through discussions with Y. Guéguen and Hoang-Trong Pho. I. Morais helped me in drafting the final manuscript. Two anonymous reviewers provided comments that greatly improved the initial manuscript. This work was supported by the Centre National de la Recherche Scientifique through the PNRN programme 'Aléa sismique—Les systèmes physiques complexes'. M. S. N. Carpenter post-edited the English style.

REFERENCES

Aggarwal, Y.P., Sykes, L.R., Armbruster, J. & Sbar, M.L., 1973. Premonitory changes in seismic velocities and prediction of earthquake, *Nature,* **241,** 101–104.

Bakun, W.H., King, G.C.P. & Cockerham, R.S., 1986. Seismic slip, aseismic slip and the mechanics of repeating earthquakes on the Calaveras fault, in *Earthquake Source Mechanics,* AGU Geophysical Monograph 37, pp. 195–207, eds Das, S., Boatwright, J. & Scholz, C. American Geophysical Union, Washington, DC.

Bosl, W.J. & Nur, A., 2002. Aftershocks and pore fluid diffusion following the 1992 Landers earthquake, *J. geophys. Res.,* **107**(B12), 2366, doi:10.1229/2001JB000155.

Brace, W.F., 1980. Permeability of crystalline and argillaceous rocks, *Abstr. Int. J. Rock. Mech. Min. Sci. Geomech.,* **17,** 241–251.

Burridge, R. & Knopoff, L., 1967. Model and theoretical seismicity, *Bull. seism. Soc. Am.,* **57,** 341–371.

Byerlee, J.D., 1979. Friction of rock, *Pure appl. Geophys.,* **116,** 615–626.

Clauser, C., 1992. Permeability of crystalline rocks, *EOS, Trans. Am. geophys. Un.,* **73**(21), 233–237.

Correig, A.M., Urquizu, M., Vila, J. & Manrubia, S., 1997. Aftershocks series of event February 18, 1996: an interpretation in terms of self-organized criticality, *J. geophys. Res.,* **102,** 27 407–27 420.

Davison, C.C. & Kozak, E.T., 1988. Hydrogeological characteristics of major fracture zones in a large granite batholith of a Canadian shield, in *Proceedings of the 4th Canadian/American Conference on Hydrogeology,* pp. 52–60, eds, Hitchon, B. & Bachu, S., National Water Well Association, Dublin, OH, USA.

Dieterich, J., 1972. Time dependent friction as a possible mechanism for aftershocks, *J. geophys. Res.,* **77,** 3771–3768.

Dieterich, J., 1994. A constitutive law for rate of earthquake production and its application to earthquakes, *J. geophys. Res.,* **99,** 2601–2618.

Douglas, J. & Rachford, H.H., 1956. On the numerical solution of heat conduction problems in two and three space variables, *Trans. Am. Math. Soc.,* **82,** 421–439.

Erickson, L., 1986. User's manual for DIS3D; a 3D dislocation program with applications to faulting in the Earth, *MS Thesis,* Stanford University, California.

Galloway, D.L., Laczniak, R., Reiner, R.L., Unger, R. & Roeloffs, E.A., 1994. Sustained aquifer fluid-pressure changes in Ash Meadows, Nevada, in response to the Northridge earthquake, *EOS, Trans. Am. geophys. Un.,* **75,** 171.

Gavrilenko, P. & Guéguen, Y., 1998. Flow in fractured media: a modified renormalization method, *Water Resources Res.,* **34,** 177–191.

Gavrilenko, P., Melikadze, G., Gibert, T.C.D. & Kumsiashvili, G., 2000. Permanent water level drop associated with the Spitak earthquake: observations at Lisi borehole (Republic of Georgia) and modelling, *Geophys. J. Int.,* **143,** 83–98.

Grecksch, G., Roth, F. & Kuempel, H.-J., 1999. Coseismic well-level changes due to the 1992 Roermond earthquake compared to static deformation of half-space solution, *Geophys. J. Int.,* **138,** 470–478.

Gross, S.J. & Kisslinger, C., 1994. Tests of models of aftershocks rate decay, *Bull. seism. Soc. Am.,* **84,** 1571–1579.

Hainzl, S., Zöller, G. & Kurths, J., 1999. Similar power laws for foreshocks and aftershock sequences in a spring block model for earthquakes, *J. geophys. Res.,* **104**, 7243–7253.

Hanks, T.C. & Kanamori, H., 1979. A moment magnitude scale, *J. geophys. Res.,* **84,** 2348–2350.

Helmstetter, A., 2002. Rupture et instabilités: sismicité et mouvements gravitaires, *PhD thesis,* J. Fourier University, Grenoble France (in English).

Hudnut, K.W. *et al.*, 1996. Co-seismic displacements of the 1994 Northridge, California earthquake, *Bull. seism. Soc. Am.,* **86,** 19–36.

King, G.C.P., Stein, R. & Lin, J., 1994. Static stress changes and the triggering of earthquakes, *Bull. seism. Soc. Am.,* **84,** 935–953.

Kisslinger, C., 1993. The stretched exponential function as an alternative model for aftershock decay rate, *J. geophys. Res.,* **98,** 1913–1922.

Kuempel, H.-J., 1992. About the potential of wells to reflect stress variations within inhomogeneous crust, *Tectonophysics,* **211,** 317–336.

Leonardi, V., Arthaud, F., Tovmassian, A. & Karakhanian, A., 1997. Relationships between seismic activity and piezometric level changes in the Arax Basin (SW Armenia): attempt at a typology of seismically induced piezometric anomalies, *Tectonophysics,* **273,** 293–316.

Li, V.C., Seale, S.H. & Cao, T., 1987. Postseismic stress and pore pressure readjustment and aftershocks distributions, *Tectonophysics,* **144,** 37–54.

Marsan, D., Bean, C.J., Steacy, S. & McCloskey, J., 2000. Observation of diffusion processes in earthquake populations and implications for the predictability of seismicity systems, *J. geophys. Res.,* **105,** 28 081–28 094.

Moreno, Y., Correig, A.M., Gomez, J.B. & Pacheco, A.F., 2001. A model for complex aftershocks sequences, *J. geophys. Res.,* **106,** 6609–6619.

Muir-Wood, R. & King, G. C.P., 1987. Hydrological signature of earthquake strain, *J. geophys. Res.,* **98,** 22 035–22 068.

Nakanishi, H., 1992. Earthquake dynamics driven by a viscous fluids, *Phys. Rev. A,* **46,** 4689–4692.

Neuman, S.P., 1994. Generalized scaling of permeabilities: validations, *Geophys. Res. Lett.,* **21,** 349–352.

Noir, J., Jacques, E., Békri, S., Adler, P.M., Tapponnier, P. & King, G. C.P., 1997. Fluid flow triggered migration of events in the 1989 Dobi earthquake sequence of central Afar, *Geophys. Res. Lett.,* **24,** 2335–2338.

Nur, A., 1972. Dilatancy, pore fluids and premonitory variations of v_s/v_p travel times, *Bull. seism. Soc. Am.,* **62,** 1217–1222.

Nur, A. & Booker, J.R., 1971. Aftershocks caused by pore fluid flow, *Science,* **175,** 885–887.

Ogata, Y., 1988. Statistical model of aftershocks temporal behaviour, *J. Am. Statist. Assoc.,* **83,** 9–27.

Ogata, Y., 1989. Statistical model for standard seismicity and detection of anomalies by residual analysis, *Tectonophysics,* **169,** 159–174.

Ogata, Y., 1992. Detection of precursory relative quiescence before great earthquakes through a statistical model, *J. geophys. Res.,* **97,** 19 845–19 871.

Okada, Y., 1992. Internal deformation due to shear and tensile faults in a half-space, *Bull. seism. Soc. Am.,* **82,** 1018–1040.

Oppenheimer, D.H., Reasenberg, P.A. & Simpson, R.W., 1988. Fault plane solutions of the 1984 Morgan Hill, California, earthquake sequence: evidence for the state of stress on the Calaveras fault, *J. geophys. Res.,* **93,** 9007–9026.

Peltzer, G., Rosen, P., Rogez, F. & Hudnut, K., 1998. Poroelastic rebound along the Landers 1992 earthquake surface rupture, *J. geophys. Res.,* **103,** 30 131–30 145.

Pride, S.R., Moreau, F. & Gavrilenko, P., 2004. Mechanical and electrical response due to fluid-pressure equilibration following an earthquake, *J. geophys. Res.,* **109,** B03302, doi:10.1029/2003JB002690.

Rice, J.R. & Cleary, M.P., 1976. Some basic stress diffusion solutions for fluid-saturated elastic porous media with compressible constituents, *Rev. Geophys. Space Phys.,* **14,** 227–241.

Roeloffs, E.A., 1998. Persistent water level changes in a well near Parkfield, California, due to local and distant earthquakes, *J. geophys. Res.,* **103,** 869–889.

Rojstaczer, S., Wolf, S. & Michel, R., 1995. Permeability enhancement in the shallow crust as a cause of earthquake-induced hydrological changes, *Nature,* **373,** 237–239.

Scholz, C., Sykes, L.R. & Aggarwal, Y.P., 1973. Earthquake prediction: a physical basis, *Science,* **181,** 803–810.

Scholz, C.H., 1968. The frequency-magnitude relation of microfracturing in rock and its relation to earthquake, *Bull. seism. Soc. Am.,* **58,** 399–415.

Stein, R.S. & Lisowski, M., 1983. The 1979 Homestead Valley earthquake sequence, California: control of aftershocks and postseismic deformation, *J. geophys. Res.,* **88,** 6477–6490.

Stein, R.S., King, G.C.P. & Lin, J., 1994. Stress triggering of the 1994 $M = 6.7$ Northridge, California, earthquake by its predecessors, *Science,* **265,** 1432–1435.

Utsu, T., Ogata, Y. & Matsu'ura, S., 1995. The centenary of the Omori formula for a decay law of aftershocks activity, *J. Phys. Earth,* **43,** 1–33.

Wang, W.-H. & Chen, C.-H., 2001. Static stress transferred by the 1999 Chi-Chi, Taiwan, earthquake: effects on the stability of the surrounding fault systems and aftershock triggering with a 3D fault-slip model, *Bull. seism. Soc. Am.,* **91,** 1041–1052.

Zoback, M.D. *et al.*, 1988. New evidence on the state of stress on the San Andreas fault system, *Science,* **238,** 1105–1111.